CrossMark

Low-temperature sintering and electric properties of BCT–BZT and BCZT lead-free ceramics

**Yongshang Tian · Yansheng Gong ·
Dawei Meng · Hao Deng · Boya Kuang**

Abstract Dielectric, ferroelectric, and piezoelectric properties between $0.33Ba_{0.8}Ca_{0.2}TiO_3$–$0.67BaTi_{1-x}Zr_xO_3$ (BCT–BZT) and $Ba_{0.934}Ca_{0.066}Ti_{1-x}Zr_xO_3$ (BCZT) lead-free ceramics, which were sintered at 1260 °C in atmosphere with different as-prepared nanoparticles, were studied. XRD results showed the evidence of the phase transitions and morphotropic phase boundary (MPB) regions of BCT–BZT and BCZT ceramics. The phase transitions in the triple point showed a sensitive variation of electric properties around MPB regions. The excellent electric properties ($\varepsilon_r = \sim 9000$, $P_r = 35.6$ μC/cm^2, and $d_{33} = \sim 240$ pC/N) were found in BCT–BZT ceramics. Spontaneous polarization states, defect dipole, and pinch effect were considered to be the important factors that influenced the electric properties. Moreover, study on the excellent electric properties around the triple point of BaTiO$_3$-based ceramics by different process would give a proposal for their practical production.

1 Introduction

Lead-based electric ceramics are extensively used in sensors, actuators, memory storage, and pyroelectric devices for their excellent piezoelectric, dielectric, and ferroelectric properties [1–4]. However, lead-based materials may cause crucial environmental pollution, which are restricted to use in the electric devices [5]. Thus, it is very urgent to find suitable lead-free materials for the substitution of lead-based materials. As we know, BaTiO$_3$ (BT) has a typical perovskite structure (ABO$_3$) with high relative permittivity (ε_r) and low loss tangent (tan δ). But the strong temperature dependence and the low Curie temperature (T_C) of BT ceramic hinder its practical application. Many researchers modified BT with isovalent cation substitution of A site and B site in ABO$_3$, such as A site by alkaline ion Ca^{2+} and Sr^{2+}, B site by Zr^{4+} and Sn^{4+} [6, 7], to improve its electric properties. Kuang et al. [8] confirmed that excellent ferroelectric properties of the substituted BT ceramics was due to the fact that Zr^{4+} was more chemical stable than Ti^{4+} [9]. Singh et al. [10] and Li et al. [11] studied the substitution of Ba^{2+} by Ca^{2+}, showing a high and stable piezoelectric properties.

As we know, the lead-based materials exhibit perfect piezoelectric and ferroelectric properties near the morphotropic phase boundary (MPB), which is very close to the phase transitions. However, MPB region wasn't found in BT-based ceramics until in 2009, when Liu and Ren firstly reported MPB region in Ba(Zr$_{0.2}$Ti$_{0.8}$)O$_3$–xBa$_{0.7}$Ca$_{0.3}$TiO$_3$ (BZT–xBCT) system [12], which was attracted much attention for their excellent piezoelectric properties ($d_{33} = 620$ pC/N) [13–15]. Hereafter, the preparation of modified BZT–xBCT materials was widely studied. Most of the researchers concerned MPB region around the rhombohedral to tetragonal phase transition point at $x = 0.5$ for their remarkable electric properties [13–19]. However, the variation of electric properties around the triple point in the phase diagram at $x = 0.33$ in BZT–xBCT system (Fig. 1) had seldom been studied.

Our previous work reported the synthesized process of BT nanoparticles by a modified Pechini polymeric precursor method [20]. The good dispersive and homogeneous BT nanoparticles not only effectively decreased the

Y. Tian · Y. Gong (✉) · D. Meng (✉) · H. Deng · B. Kuang
Faculty of Material Science and Chemistry, China University of Geosciences, Wuhan 430074, People's Republic of China
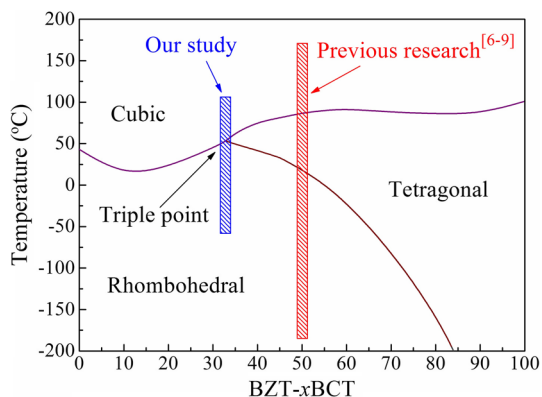e-mail: gongysh@cug.edu.cn

D. Meng
e-mail: dwmeng@cug.edu.cn

Fig. 1 Phase diagram of BZT–xBCT system

sintered temperature (~1500 °C in conventional solid re-action process), but also refrained from weakening electric properties of BT-based ceramics. In the present study, the as-prepared $0.33Ba_{0.8}Ca_{0.2}TiO_3$–$0.67BaTi_{1-x}Zr_xO_3$ (BCT–BZT) and $Ba_{0.934}Ca_{0.066}Ti_{1-x}Zr_xO_3$ (BCZT) nanoparticles and ceramics were prepared. The comparison of dielectric, ferroelectric, and piezoelectric properties between BCT–BZT and BCZT lead-free ceramics in different synthesized process were explored. In addition, the phase transitions and the densification near the triple point of BCT–BZT and BCZT ceramics were studied in detail.

2 Experimental

The as-prepared $Ba_{0.8}Ca_{0.2}TiO_3$ (BCT), $BaTi_{1-x}Zr_xO_3$ (BZT, $x = 0$; 0.01; 0.025; 0.04; 0.05; 0.10; 0.20), and $Ba_{0.934}Ca_{0.066}Ti_{1-x}Zr_xO_3$ (BCZT, $x = 0$; 0.0067; 0.01675; 0.0268; 0.0335; 0.067; 0.134) nanoparticles were synthesized by a modified Pechini polymeric precursor method. The stoichiometric mixed $0.33Ba_{0.8}Ca_{0.2}TiO_3$–$0.67BaTi_{1-x}Zr_xO_3$ (BCT–BZT) and BCZT nanoparticles were dispersed homogeneously and then pressed into disk-shaped discs of 20 mm in diameter by using 5 wt% polyvinyl alcohol (PVA) binder under 150 MPa pressure. After burning out PVA at 650 °C, the green bodies were finally sintered at 1260 °C for 5 h in air atmosphere for the ceramics.

The crystal structure was measured by X-ray diffraction (XRD, X'Pert PRO) with Cu-Kα radiation at room-temperature. The precision electronic balance (ED-124S) was used to confirm the densification of the ceramics by Archimedes immersion principle. The fractured microstructure of the ceramics was examined by field emission scanning electron microscopy (FESEM, SUV-1080). The samples were polished and silver electrodes were painted in both circular faces and annealed at 600 °C for 30 min for the dielectric and piezoelectric measurements. Before measuring the piezoelectric properties, the sintered

ceramics were poled in silicone oil bath under an electric field of 25 kV/cm at 25 °C for about 40 min. The permittivity (ε_r) and loss tangent (tan δ) value were carried out with a frequency of 10 kHz using a precision LCR meter (TH-2819). The resonance (f_r) and anti-resonance (f_a) frequency of poled ceramics were measured by precision impedance analyzer (Agilent-4292A), and the electromechanical coupling factors (k_p) and mechanical quality factor (Q_m) were calculated using Onoe and Jumonji formula [21, 22]. Piezo-d_{33} meter (ZJ-3A) was used to test the piezoelectric constant (d_{33}) of ceramics. The polarization versus electric field (P–E) hysteresis loops of the ceramics were measured using a radiant precision workstation (Premier II) at 20 Hz.

3 Results and discussion

Figure 2 shows the XRD patterns of BZT nanoparticles in the 2θ range of 10°–70° with various zirconium content (x). According to the results, a pure rhombohedral perovskite phase was found except $x = 0$ (coexisted rhombohedral with tetragonal phase), which was consistent well with JCPDS # 85-1796. From the expanded XRD patterns in Fig. 2b in the 2θ range of 43°–47°, it was observed that the (200) diffraction peak position shifted monotonically to low 2θ angle with increasing x, which was due to the fact that the ionic radius of Zr^{4+} (0.087 nm) was larger than Ti^{4+} (0.068 nm) in BZT lattice [23]. The merged (200) diffraction peak at ~45° confirmed the evolvement of phase transition from tetragonal to rhombohedral at room temperature with increasing x. The main diffraction peaks receded with increasing x, which derived from the limited solid solubility or the substitution with A/B position in perovskite structure (ABO_3) [24, 25]. Figure 3 shows the
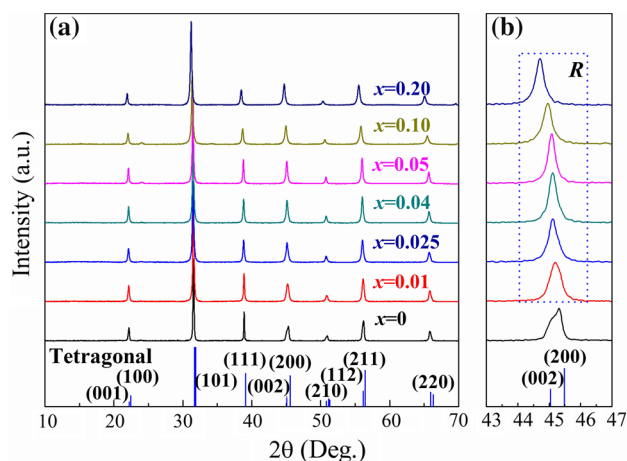

Fig. 2 XRD patterns (**a**) and selected enlarged regions of 43°–47° (**b**) of BZT nanoparticles with various zirconium content (x)

XRD patterns of BCZT nanoparticles with different x. There was no secondary phase in the 2θ range of $10°$–$70°$, showing a pure rhombohedral phase. The shifty tendency of diffraction peak position in BCZT nanoparticles was also attributed to the substitution of smaller ion Ti^{4+} by larger ion Zr^{4+} in BCZT lattice.

Figure 4 shows the XRD patterns of BCT–BZT ceramics in the 2θ range of $10°$–$70°$ with various zirconium content (x). All the ceramics showed a perovskite structure phase, and no secondary phase was observed. As shown in the selected enlarged regions of XRD patterns in Fig. 4b, the unique splitting (022) and (200) diffraction peaks of orthorhombic (JCPDS # 81-2200) phase receded gradually and merged into (200) diffraction peak of rhombohedral phase with increasing x, and (022) diffraction peak of orthorhombic phase disappeared completely when x was
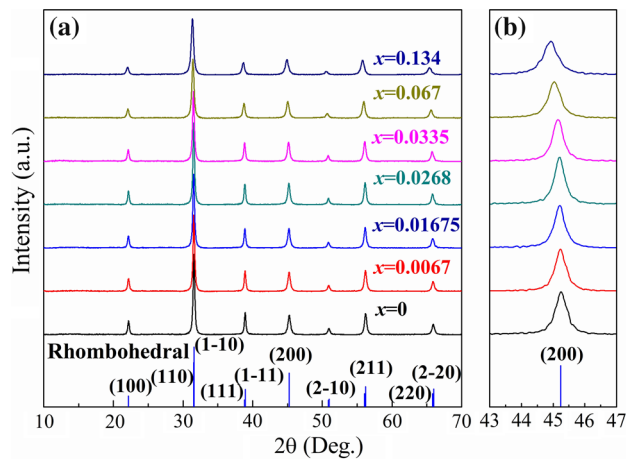
raised to 0.05. From Fig. 4b, BCT–BZT ceramics showed a single orthorhombic phase when $x < 0.025$, the coexistence of orthorhombic and rhombohedral phases (O–R) appeared in x range of 0.04–0.05, while a single rhombohedral phase was obtained in x range of 0.10–0.20. Some diffraction peaks intensity weakened subtly with increasing x, which was attributed to the limited solid solubility in the ABO_3 structure. The variation of diffraction peaks position in low 2θ value was due to the fact that the substitution of smaller ion Ti^{4+} by larger ion Zr^{4+} of B position in ABO_3, resulting in an enlargement of BCT–BZT lattice.

XRD patterns with various x in BCZT ceramics were showed in Fig. 5. The element contents of BCZT ceramics were equivalent with BCT–BZT ceramics in Fig. 4. The results showed that the (002) and (200) diffraction peaks of single tetragonal phase weakened gradually with increasing x in the range of 0–0.0067. An interesting transformation from tetragonal (JCPDS # 05-0626) to orthorhombic symmetry was found at $x > 0.0067$, and a coexistence of tetragonal and orthorhombic phases (T–O) of BCZT ceramics was found at $x = 0.01675$. The (002) and (200) diffraction peaks of tetragonal phase changed into (220) and (200) diffraction peaks in single orthorhombic phase at $x = 0.0268$. Then, a transformation from orthorhombic to rhombohedral phase with increasing x was detected. The coexisted orthorhombic and rhombohedral phases (O–R) were confirmed at $x = 0.0335$, and the single rhombohedral phase was found at x range of 0.067–0.134. Thus, it can be concluded that the MPB regions of BCZT ceramics may exist at x around 0.01675 (T–O), and 0.0335 (O–R). However, the MPB region of BCT–BZT ceramics was only found in x range of 0.04–0.05 (O–R) as showed in Fig. 4. Comparing with the diffraction peaks intensity of BCT–BZT (Fig. 4) and BCZT (Fig. 5) ceramics, the preparation

Fig. 3 XRD patterns (a) and selected enlarged regions of $43°$–$47°$ (b) of BCZT nanoparticles with various zirconium content (x)
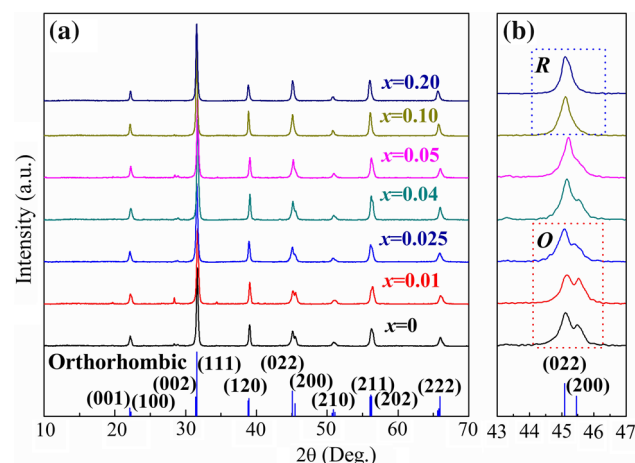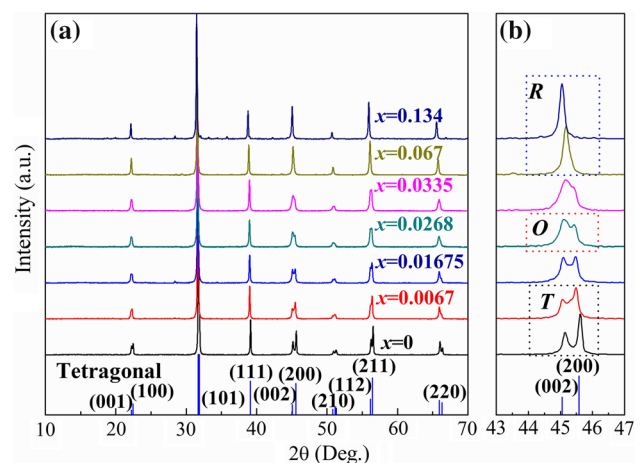

Fig. 4 XRD patterns of BCT–BZT ceramics with various zirconium content (x). a Wide range, b selected enlarged regions of $43°$–$47°$

Fig. 5 XRD patterns of BCZT ceramics with various zirconium content (x). a Wide range, b selected enlarged regions of $43°$–$47°$
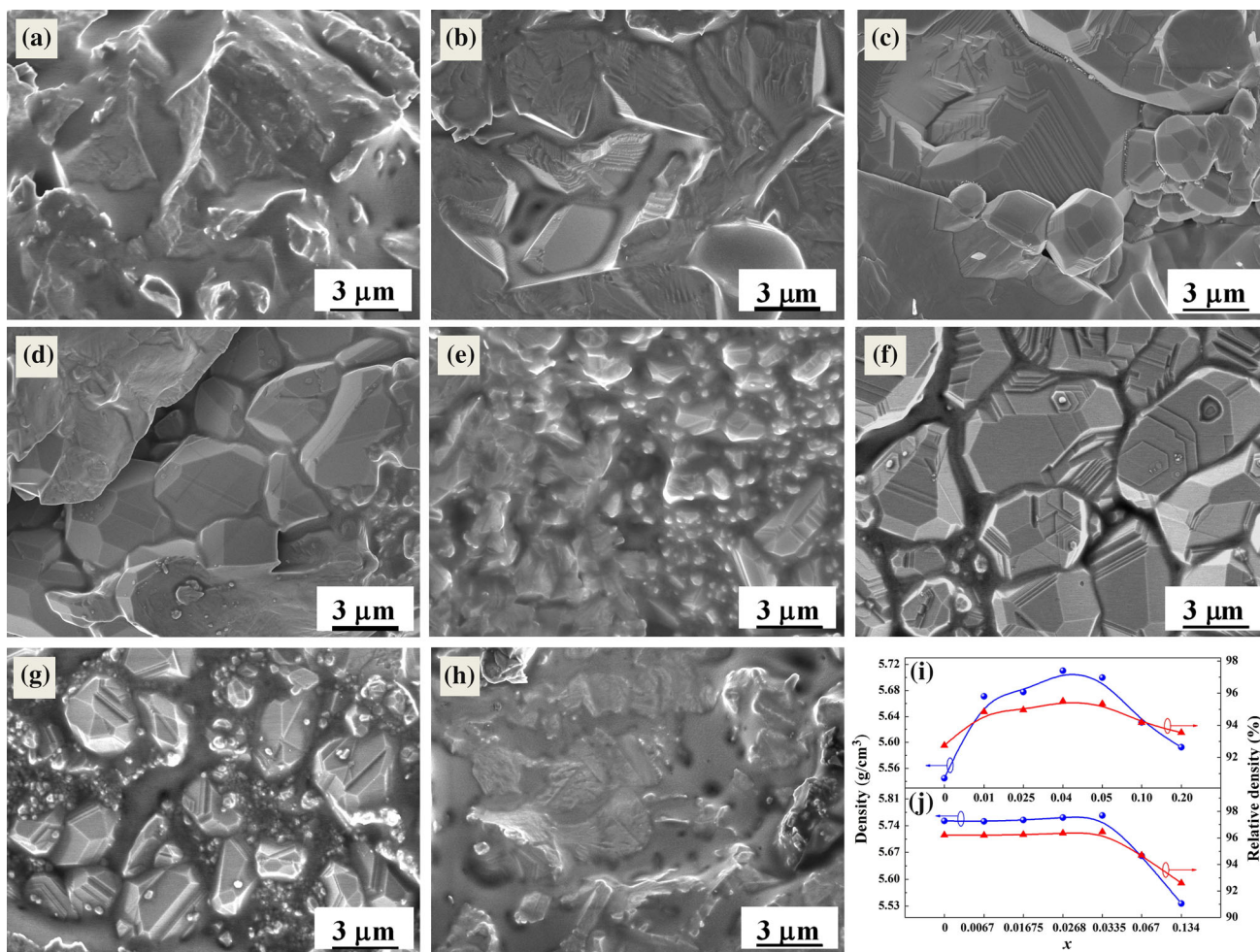
Fig. 6 FESEM morphology of BCT–BZT ceramics with zirconium content (x) at **a** 0, **b** 0.04, **c** 0.05, **d** 0.1; and BCZT ceramics with zirconium content (x) at, **e** 0, **f** 0.01675, **g** 0.0335, **h** 0.67. Density and relative density of, **i** BCT–BZT ceramics and, **j** BCZT ceramics with various zirconium content (x)

of BCZT ceramics with nanoparticles had a higher crystallinity at the sintering temperature of 1260 °C.

Figure 6a–d indicates the FESEM images of BCT–BZT ceramics microstructure with various zirconium content (x) of (a) = 0, (b) = 0.04, (c) = 0.05; (d) = 0.10. The grain size of BCT–BZT ceramics increased obviously with increasing x, and there existed fine and small crystal grains in the BCT–BZT ceramic boundary at $x = 0.05$. All of the BCT–BZT ceramic grain size (~ 3 μm) was smaller than the literature [13, 26, 27]. The small grains and dense microstructure not only improved the densification of BCT–BZT ceramics (Fig. 6i), but also enhanced the piezoelectric properties [28]. From the fracture surface feature of BCT–BZT ceramics, it was observed that the fracture mode changed from transgranular to intergranular fracture, which was associated with the fine grains with increasing x [29]. Figure 6e–h shows the FESEM images of the fractured surfaces of BCZT ceramics with various

zirconium content (x) of (e) = 0, (f) = 0.01675, (g) = 0.0335; (h) = 0.067. The dense ceramic microstructure and grain morphology were dependent on x largely. There also existed transgranular fracture as x was raised to 0.067, which was attributed to the sufficient grain growth of BCZT ceramics prepared with the nanoparticles.

Figure 6i, j indicates the density and relative density of BCT–BZT and BCZT ceramics with various zirconium content (x). It was observed that the density and relative density of BCT–BZT and BCZT ceramics increased firstly and then decreased with increasing x. The relative density of BCT–BZT ceramics reached to 95.5 % at $x = 0.04$ in Fig. 6i, and the relative density of BCZT ceramics (96.3 %) was a little higher than BCT–BZT ceramics at the equal zirconium content of $x = 0.0268$ in Fig. 6j, which was ascribed to the different nanoparticles. The density variations of BCT–BZT and BCZT ceramics might be attributed to the phase transition, which were consistent well

with the results in Figs. 4 and 5. All the BCT–BZT and BCZT ceramics sintered at 1260 °C had a high relative density, showing an appropriate route to prepare the ceramics with nanoparticles at low sintering temperature, which was beneficial for their practical application.

Figure 7 shows the temperature dependence of the permittivity (ε_r) and the loss tangent (tan δ) for the unpoled BCT–BZT and BCZT ceramics with different zirconium content (x). Figure 7a indicated that the peaks of the permittivity in ε_r-T curves near T_C broadened, and the permittivity value increased with a small addition of zirconium. However, the maximum value of permittivity (ε_m) and T_C decreased apparently when x was raised to 0.20, which were attributed to the structural distortions and were consistent well with Choi et al. [24] results. Figure 7a also indicates the dielectric peaks corresponded to the transition temperature from orthorhombic to tetragonal phase (T_{O-T}), and the T_{O-T} showed clearly at $x = 0.04$–0.05. The phase transformation was consistent well with the result in Fig. 4. However, due to the pinched phase transition, the T_{O-T} wasn't found at higher x, and the transition of rhombohedral to orthorhombic phase (T_{R-O}) was not clear [30]. The dielectric peak value and T_C (Fig. 7c) decreased with higher x, showing a dielectric relaxation behavior, which was associated with the weakened B–O band in the ABO_3 structure, and it was difficult for B-site ion to resume in rhombohedral or orthorhombic phase [8]. From the loss tangent results in Fig. 7a, tan δ was higher than the literature, which might be ascribed to the finer grain size and more grain boundaries at the setting conditions [31].

A similar variation tendency of ε_r and tan δ of unpoled BCZT ceramics were also found in Fig. 7b. The maximum dielectric value was about 5600 at $x = 0.0335$, but it was quite lower than ε_r ($\sim$9000) of BCT–BZT ceramic in Fig. 7a, which was attributed to the larger grain size in BCZT ceramics than in BCT–BZT ceramics (Fig. 6). However, the tan δ of BCZT ceramics was relative lower than that of BCT–BZT ceramics, which was due to the higher densification of the ceramics by the homogeneous nanoparticles [32]. The lowest tan δ was found and T_{O-T} was showed clearly as $x = 0.0335$ in BCZT ceramics, the reason for the results were stated above. The variation of loss tangent peaks in Fig. 7a, b revealed the transformation from ferroelectric to paraelectric phase in BCT–BZT and BCZT ceramics, which was consistent well with the change of permittivity. Figure 7c, d indicates the variation of T_C of BCT–BZT and BCZT ceramics with increasing zirconium content (x). It was shown that T_C value dropped abruptly with the excessive addition of zirconium, which might be attributed to the weakened bonding force between B-site and oxygen ion in ABO_3 structure, leading to the distortion of octahedron structure after excessive
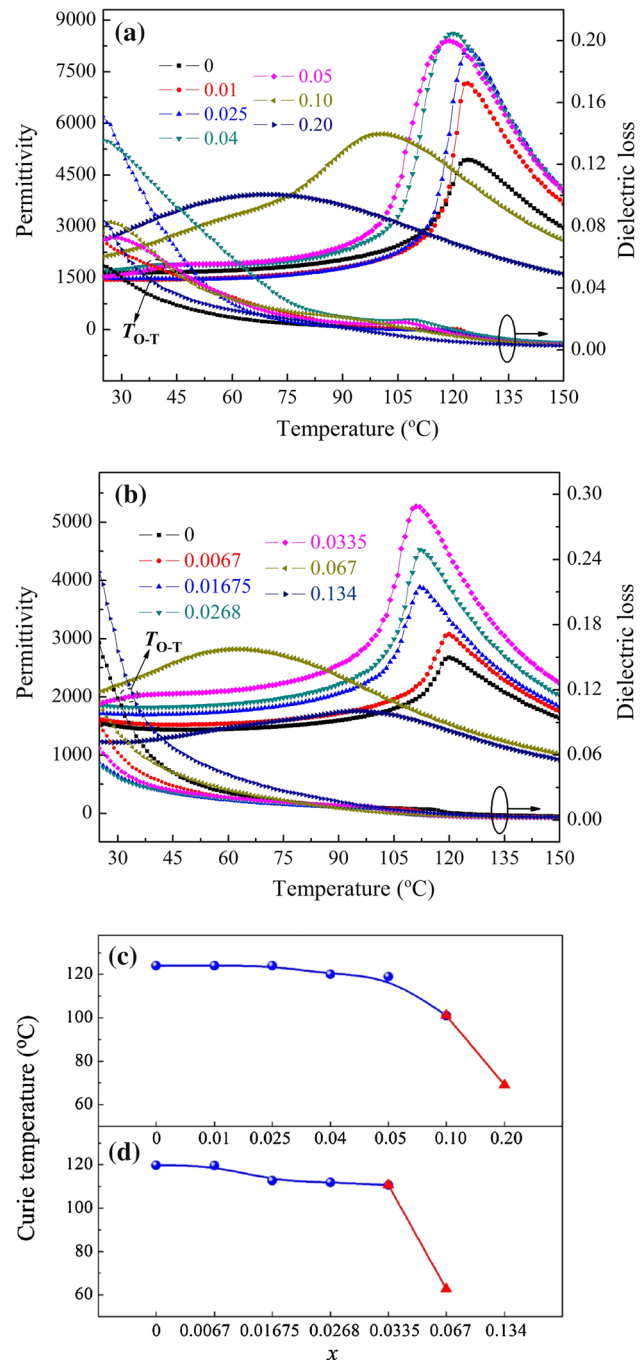

Fig. 7 Temperature dependence of permittivity (ε_r) and loss tangent (tan δ) of **a** BCT–BZT ceramics, **b** BCZT ceramics with different zirconium content (x) at 10 kHz, and, **c** variation of the Curie temperature (T_C) of BCT–BZT and BCZT ceramics with different zirconium content (x)

substitution of Ti^{4+} ion, and showing a dependence of T_C with x [8, 33].

Figure 8a shows the P–E hysteresis loops of BCT–BZT ceramics with different zirconium content (x) at room temperature. All the ceramics exhibited a typical saturated
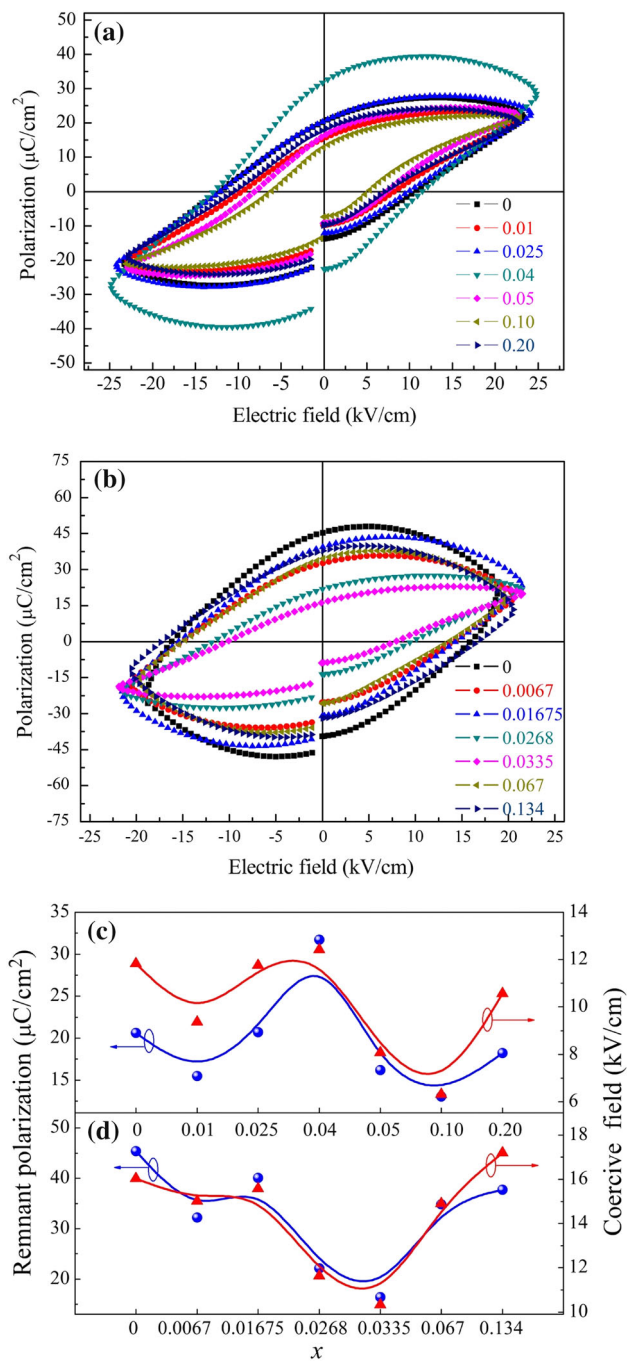
Fig. 8 P–E hysteresis loops of, **a** BCT–BZT ceramics, **b** BCZT ceramics with different zirconium content (x), and, **c** variation of remanent polarization (P_r) and coercive field (E_c) of BCT–BZT and BCZT ceramics with different zirconium content (x)

hysteresis loop under the setting electric field. Variations of the remnant polarization (P_r) and coercive field (E_c) were shown in Fig. 8c. P_r and E_c showed a similar variation trend with increasing x, which didn't totally confirm with the literature reports [23, 27, 33]. The reason for the maximum of $P_r = 35.6$ μC/cm² at $x = 0.04$ was associated with the improved spontaneous polarization in the coexisted phases

around the triple point of BZT–xBCT system. However, the larger E_c was also found around MPB regions, which might be associated with the fact that there existed defect dipoles, and provided a restoring force at the setting electric field [34]. As the BCT–BZT ceramics were sintered by BCT and BZT nanoparticles, there might exist inhomogeneous phases in the grain or grain boundary, resulting in the different domain regions in the ceramics and higher E_c. The similar results were also revealed in the P–E hysteresis loops of BCZT ceramics (Fig. 8b). However, some of the hysteresis loops were not well-saturated under the examined electric field, which might be ascribed to the finer grains and more grain boundary. The higher P_r and E_c were found at $x = 0.01675$, the reasons were stated above. But, the lowest P_r and E_c were found when x was reached to 0.0335 (O–R MPB regions) in Fig. 8b, the lowest E_c might result from the easier domain reorientation in MPB region, and the lowest P_r might be attributed to the relative lower testing temperature. The unsaturated hysteresis loops in Fig. 8b demonstrated a higher leakage current, which may guide the synthesis process of BCZT ceramics.

Figure 9 shows the piezoelectric constant (d_{33}), electromechanical coupling factors (k_p) and mechanical quality factor (Q_m) of BCT–BZT and BCZT ceramics with different zirconium content (x) at room temperature. The lowest Q_m in BCT–BZT ceramics was found at $x = 0.04$ and Q_m in BCZT ceramics attained the minimum value at $x = 0.0268$, which was ascribed to the decreasing internal stress in MBP regions [12–14]. The maximum value of Q_m was found at $x = 0.1$ in BCT–BZT ceramics and $x = 0.067$ in BCZT ceramics, which were attributed to the large pinch effect in domain wall [35, 36]. However, Q_m of the ceramics dropped sharply at higher x, which might be due to the little pinch effect in the
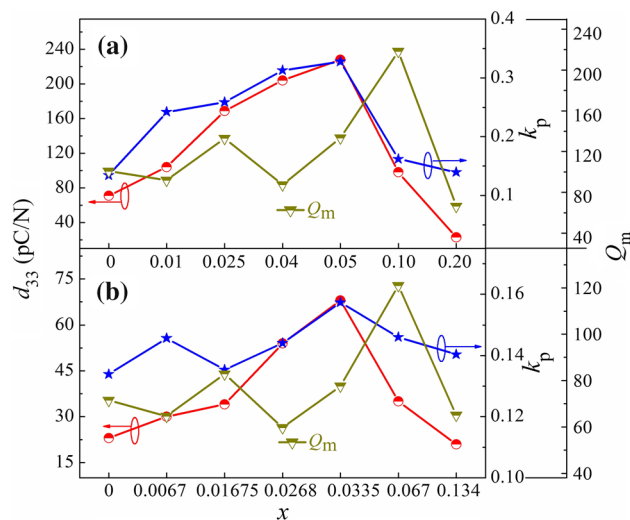

Fig. 9 Piezoelectric constant (d_{33}), electromechanical coupling factors (k_p) and mechanical quality factor (Q_m) of BCT–BZT and BCZT ceramics with various zirconium content (x)

large grain size [37]. From the results in Fig. 9, d_{33} and k_p value of BCT–BZT and BCZT ceramics increased firstly and then decreased with increasing x, the highest d_{33} and k_p appeared close to the MPB region, in which there were more spontaneous polarization states than that of the single phase region [16–19]. The d_{33} and k_p value of BCT–BZT ceramics were all higher than that of in BCZT ceramics, which might be attributed to the more easier polarization reversion in the MPB regions. Moreover, the highest d_{33} (~ 240 pC/N) of BCT–BZT ceramic showed much better piezoelectric properties than that of in the BCZT ceramics (~ 75 pC/N). The different process of synthesized BCT–BZT and BCZT ceramics with various electric properties offered a guidance for the preparation of promising lead-free materials at a low sintering temperature.

4 Conclusions

$0.33Ba_{0.8}Ca_{0.2}TiO_3$–$0.67BaTi_{1-x}Zr_xO_3$ and $Ba_{0.934}Ca_{0.066}$ $Ti_{1-x}Zr_xO_3$ (BCZT) lead-free ceramics were synthesized with different nanoparticles by a modified Pechini polymeric precursor method, and sintered at 1260 °C in atmosphere. The homogeneous nanoparticles enhanced the ceramics densification and the grain dimension. XRD results confirmed the MPB region (T–O) in zirconium content (x) range of 0.04–0.05 in BCT–BZT ceramics, and MPB regions (T–O and O–R) appeared at x around 0.01675 and 0.0335 in BCZT ceramics. The enhanced ferroelectric and piezoelectric properties around the MPB regions showed a sensitive dependence on zirconium content. BCT–BZT ceramics had a higher electric properties ($\varepsilon_r = \sim 9000$; $P_r = 35.6$ μC/cm^2; $d_{33} = \sim 240$ pC/N; $k_p = 0.34$) than that of in BCZT ceramics ($\varepsilon_r = \sim 5600$; $d_{33} = \sim 75$ pC/N; $P_r = 18.7$ μC/cm^2; $k_p = 0.16$), but lower crystallinity and smaller grain size. Furthermore, the research on the pinch effect, B-site effect in ABO_3, and defect dipole effect on the triple point of BZT–xBCT system would promote the practical production of BT-based materials.

References

1. B. Jaffe, W. Cook, H. Jaffe, *Piezoelectric Ceramics* (Academic Press, London, 1971), pp. 185–212
2. X.G. Tang, H.Y. Tian, J. Wang, K.H. Wong, H.L.W. Chan, Appl. Phys. Lett. **89**, 142911 (2006)
3. E. Dul'kin, E. Mojaev, M. Roth, W. Jo, T. Granzow, Scr. Mater. **60**, 251 (2009)
4. J.H. Yoo, K.H. Yoo, Y.W. Lee, S.S. Suh, J.S. Kim, C.S. Yoo, Jpn. J. Appl. Phys. **39**, 2680 (2000)
5. J. Rödel, W. Jo, K.T.P. Seifert, E.M. Anton, T. Granzow, D. Damjanovic, J. Am. Ceram. Soc. **92**, 1153 (2009)
6. Y.L. Wang, L.T. Li, J.Q. Qi, Z.L. Gui, Ceram. Int. **28**, 657 (2002)
7. J.G. Wu, A. Habibul, X.J. Cheng, X.P. Wang, B.Y. Zhang, Mater. Res. Bull. **48**, 4411 (2013)
8. S.J. Kuang, X.G. Tang, L.Y. Li, Y.P. Jiang, Q.X. Liu, Scr. Mater. **61**, 68 (2009)
9. X.G. Tang, J. Wang, X.X. Wang, H.L.W. Chan, Solid State Commun. **131**, 163 (2004)
10. G. Singh, V.S. Tiwari, P.K. Gupta, Appl. Phys. Lett. **102**, 162905 (2013)
11. W. Li, Z.J. Xu, R.Q. Chu, P. Fu, G.Z. Zang, J. Am. Ceram. Soc. **94**, 4131 (2011)
12. W.F. Liu, X.B. Ren, Phys. Rev. Lett. **103**, 257602 (2009)
13. I. Coondoo, N. Panwar, H. Amorín, M. Alguero, A.L. Kholkin, J. Appl. Phys. **113**, 214107 (2013)
14. Q.W. Zhang, H.Q. Sun, X.S. Wang, Y. Zhang, X. Li, J. Eur. Ceram. Soc. **34**, 1439 (2014)
15. M.C. Ehmke, N.H. Khansur, J.E. Daniels, J.E. Blendell, K.J. Bowman, Acta Mater. **66**, 340 (2014)
16. A.B. Haugen, J.S. Forrester, D. Damjanovic, B. Li, K.J. Bowman, J.L. Jones, J. Appl. Phys. **113**, 014103 (2013)
17. D.Z. Xue, Y.M. Zhou, H.X. Bao, C. Zhou, J.H. Gao, X.B. Ren, J. Appl. Phys. **109**, 054110 (2011)
18. J.H. Gao, D.Z. Xue, Y. Wang, D. Wang, L.X. Zhang, H.J. Wu, S.W. Guo, H.X. Bao, C. Zou, W.F. Liu, S. Hou, G. Xiao, X.B. Ren, Appl. Phys. Lett. **99**, 092901 (2011)
19. Q.W. Zhang, H.Q. Sun, Y. Zhang, J. Am. Ceram. Soc. **97**, 868 (2013)
20. Y.S. Tian, Y.S. Gong, Z.L. Zhang, D.W. Meng, J. Mater. Sci. Mater. Electron. **25**, 5467 (2014)
21. M. Onoe, H. Jumonji, J. Acoust. Soc. Am. **41**, 974 (1967)
22. S. Gurvinderjit, V.S. Tiwari, P.K. Gupta, Appl. Phys. Lett. **102**, 162905 (2013)
23. J.G. Wu, D.Q. Xiao, W.J. Wu, Q. Chen, J.G. Zhu, Z.C. Yang, J. Wang, J. Eur. Ceram. Soc. **32**, 891 (2012)
24. Y.K. Choi, T. Hoshina, H. Takeda, T. Tsurumi, J. Ceram. Soc. Jpn. **118**, 881 (2010)
25. C.Y. Chang, H.I. Ho, T.Y. Hsieh, C.Y. Huang, Y.C. Wu, Ceram. Int. **39**, 8245 (2013)
26. J.G. Wu, D.Q. Xiao, B. Wu, W.J. Wu, J.G. Zhu, Z.C. Yang, Mater. Res. Bull. **47**, 1281 (2012)
27. S.W. Zhang, H.L. Zhang, B.P. Zhang, S. Yang, J. Alloys Compd. **506**, 131 (2010)
28. J.G. Wu, W.J. Wu, D.Q. Xiao, J. Wang, Z.C. Yang, Z.H. Peng, Q. Chen, J.G. Zhu, Curr. Appl. Phys. **12**, 534 (2012)
29. S. Mahajan, O.P. Thakur, D.K. Bhattacharya, K. Sreenivas, Mater. Chem. Phys. **112**, 858 (2008)
30. Y. Zhi, A. Chen, R. Guo, A.S. Bhalla, Mater. Lett. **61**, 326 (2007)
31. X.G. Tang, K.H. Chew, H.L.W. Chan, Acta Mater. **52**, 5177 (2004)
32. S.G. Lee, D.S. Kang, Mater. Lett. **57**, 1629 (2003)
33. W. Lin, L.L. Fan, D.M. Lin, Q.J. Zheng, X.M. Fan, H.L. Sun, Curr. Appl. Phys. **13**, 159 (2013)
34. P.F. Zhou, B.P. Zhang, L. Zhao, X.K. Zhao, L.F. Zhu, L.Q. Cheng, J.F. Li, Appl. Phys. Lett. **103**, 172904 (2013)
35. L.X. Zhang, X.B. Ren, Phys. Rev. B **73**, 094121 (2006)
36. O.P. Thakur, C. Prakash, A.R. James, J. Alloys Compd. **470**, 548 (2009)
37. M.C. Ehmke, J. Daniels, J. Glaum, M. Hoffman, J.E. Blendell, K.J. Bowman, J. Am. Ceram. Soc. **96**, 2913 (2013)